Check for updates

Hard templating ultrathin polycrystalline hematite nanosheets: effect of nano-dimension on CO_2 to CO conversion *via* the reverse water-gas shift reaction†

Zachary S. Fishman, [ID] [a] Yulian He,[a] Ke R. Yang,[b] Amanda W. Lounsbury,[a] Junqing Zhu,[c] Thanh Minh Tran,[a] Julie B. Zimmerman,[a] Victor S. Batista*[b] and Lisa D. Pfefferle*[a]

Understanding how nano-dimensionality impacts iron oxide based catalysis is central to a wide range of applications. Here, we focus on hematite nanosheets, nanowires and nanoparticles as applied to catalyze the reverse water gas shift (RWGS) probe reaction. We introduce a novel approach to synthesize ultrathin (4–7 nm) hematite nanosheets using copper oxide nanosheets as a hard template and propose a reaction mechanism based on density functional theory (DFT) calculations. Hematite nanowires and nanoparticles were also synthesized and characterized. H_2 temperature programmed reduction (H_2-TPR) and RWGS reactions were performed to glean insights into the mechanism of CO_2 conversion to CO over the iron oxide nanomaterials and were compared to H_2 binding energy calculations based on density functional theory. While the nanosheets did exhibit high CO_2 conversion, 28% at 510 °C, we found that the iron oxide nanowires had the highest CO_2 conversion, reaching 50% at 750 °C under atmospheric pressure. No products besides CO and H_2O were detected.

Introduction

Hematite is a nontoxic, stable iron oxide composed of earth abundant elements with a wide array of applications in water splitting,[1] adsorption of metals,[2] and other fields. For many processes, such as catalysis, electrochemistry and photovoltaics, significant improvements in performance can be realized by increasing surface area or by changing the optoelectronic properties of the material. Therefore, it is of great interest to understand how the size and morphology of nano-hematite particles affect their structural and functional properties.[3–5]

Though much work has been done towards characterizing 0D and 1D systems, only a few reports have investigated 2D hematite (*i.e.* nanosheets). Iron oxide nanosheets doped with silicon,[6] germanium,[7,8] sodium, and potassium[9] have exciting photo(electro)chemical properties. Additionally, other groups have synthesized iron hydroxides, which have unique magnetic

properties ideal for spintronics.[10] Still left unstudied, though, is the undoped hematite nanosheet system, and how the properties of the 2D material compares to its 0D and 1D analogues.

Difficulties in synthesis have hindered earlier studies. Here, we implement templating, which is a common wet chemistry technique for nanomaterial synthesis because it is simple, reproducible, and inexpensive. Soft templates, such as surfactants and polymers, self-assemble under certain solution conditions into micelles and lamellar phases that have been used to synthesize a wide array of 0D,[11] 1D,[12,13] and 2D[14,15] nanomaterials. Though flexible, the structure of soft templates can also act as a disadvantage because they place additional restrictions on the conditions of the reaction. In addition, variables such as pH and temperature, which govern the kinetics of nanomaterial growth, also change the structure of the soft template.[11] Such a co-dependence poses a challenge for studies of nanoparticle formation and development of synthetic protocols.

An alternative to the soft templating approach is the use of hard templates. Unlike soft templates, the structure of hard templates is not sensitive to changes in the solution environment. Mesoporous silica, alumina membranes, and ion-track etched membranes have been used to synthesize carbon nanotubes,[16] boron nanotubes,[17] nickel nanowires,[18] Au nanorods, and TiO_2 nanoparticles.[19] Though stable in solution, hard

*a*Department of Chemical and Environmental Engineering, Yale University, New Haven, Connecticut 06520-8286, USA. E-mail: lisa.pfefferle@yale.edu
*b*Department of Chemistry and Energy Sciences Institute, Yale University, New Haven, Connecticut 06520-8107, USA. E-mail: victor.batista@yale.edu
*c*Department of Chemistry, Nankai University, Tianjin 300071, China
†Electronic supplementary information (ESI) available: Additional characterization of nanomaterials including SEM, TEM, and AFM images; XRD, FTIR, and EDX spectroscopy; and mass spectrometry. See DOI: 10.1039/c7nr03522e

templates are harder to remove[18] and have been mostly used as a mold to synthesize 0D and 1D structures. Unfortunately, due to geometric constraints, the mold approach is not feasible for 2D nanomaterial synthesis. Therefore, a new class of hard templates needs to be developed.

Growing nanomaterials on other nanomaterials, compositing, is becoming quite common for development of catalysts,[20] high surface area adsorbents,[21] improved batteries,[22] or composites with unique properties.[23,24] For example, graphene and other materials are frequently used as templates for other nanomaterial growth. Graphene oxide has been shown to function as a self-sacrificial hard template for MnO_2 synthesis.[25] Here, we use copper oxide (CuO) nanosheets as a growth template for synthesizing 2D iron oxides and hydroxides. We demonstrate that the hard CuO template is easily removable. We compare the synthesized hematite nanosheets with hematite nanowires and hematite nanoparticles to study the effects of nano-dimension on the catalytic conversion of CO_2 to CO via the reverse water gas shift reaction.

Many emerging technologies are currently geared toward CO_2 conversion, motivated by current environmental concerns. Beyond Earth, there is also a strong incentive for CO_2 utilization in space exploratory programs, including CO_2 capture and utilization during long-term missions and exploration of planets with a CO_2 rich atmosphere. Electrochemical and photocatalytic methods are the most commonly explored reaction pathways for CO_2 conversion. In addition, catalytic CO_2 hydrogenation via the reverse water gas shift reaction, shown in eqn (1), is gaining significant attention:

$$CO_{2(g)} + H_{2(g)} \rightarrow H_2O_{(g)} + CO_{(g)}. \tag{1}$$
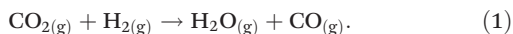
CO is a critical component of synthesis gas ("syngas"), which can, in turn, be used to synthesize an array of useful chemicals via the Fisher–Tropsch reaction. In the past, other groups have studied the RWGS reaction over catalysts composed of Fe–, Co–, Ni– on alumina,[26,27] molybdenum and tungsten disulfides,[27] Pt,[28] copper and nickel ferrites,[29] and other iron containing materials.[30] Many groups have shown promising results, however many challenges still persist: (1) high conversion efficiencies are currently achieved at the cost of selectivity; (2) low operating temperatures are possible only by using rare earth metals, such as platinum or palladium; and (3) almost all of these processes require high pressure and highly pure CO_2. Here, we demonstrate the use of iron oxide nanomaterials as low cost, highly selective catalysts for reverse water gas shift at atmospheric pressure.

Experimental

Synthesis of 6-line ferrihydrite and hematite nanosheets

6-Line ferrihydrite and hematite nanosheets were grown using copper oxide nanosheets as a hard template. A solution based surfactant soft templating procedure was used to first synthesize copper oxide nanosheets, as detailed in our previous work.[31] In a typical synthesis for 6-line ferrihydrite and hema-

tite nanosheets, 900 mg of CuO nanosheets were dispersed in 900 mL of deionized water using magnetic stirring. The solution was then heated to 60 °C, at which point 3.4 g of iron(II) sulfate heptahydrate [$FeSO_4 \cdot 7H_2O$] was dissolved in the solution under magnetic stirring. After 2 h the color of the solution changed from black to dark orange. The precipitate was then separated by filtration and washed with excess deionized water to remove unreacted iron precursor ions. To remove the CuO nanosheets the precipitate was washed three times with 300 ml of concentrated ammonium hydroxide (28.0–30.0%), or until the filtrate was no longer blue. The remaining orange sample was then washed with DI-water, vacuum dried and crushed using mortar and pestle before further characterization and treatment. To transform the sample into hematite, the nanosheets were subsequently heated in air at 400 °C for 30 minutes.

Synthesis of goethite and hematite nanowires

First, 60 g of sodium hydroxide was dissolved in 450 ml of deionized water and the solution was heated to 50 °C. In parallel, 1.95 g iron(II) sulfate heptahydrate [$FeSO_4 \cdot 7H_2O$] was dissolved in 50 ml of deionized water. N_2 was then bubbled through both solutions for 30 minutes to purge the dissolved oxygen. After 30 minutes, the iron sulfate solution was added to sodium hydroxide solution and allowed to react for 1 hour at 50 °C under magnetic stirring and N_2 bubbling. Temperature was carefully controlled to prevent the formation of magnetite nanoparticles via the Schikorr reaction. The green precipitate was then filtered and washed with excess deionized water under an N_2 blanket and subsequently vacuum dried and crushed using mortar and pestle. To transform the sample into hematite, the nanowires were subsequently heated in air at 400 °C for 15 minutes.

Synthesis of hematite nanoparticles

Nano-hematite particles were synthesized using a modified version of Schwertmann and Cornell's Iron Oxides in the Laboratory hematite synthesis method 3.[32] The modification was such that 10.86 g of $FeCl_3 \cdot 6H_2O$ was added to 2 L of 0.002 M HCl pre-heated to 90 °C. Once the $FeCl_3$ salt was dissolved the 2 L solution was baked at 97 °C ± 1 °C for 7 days.

Scanning electron microscopy (SEM), transmission electron microscopy (TEM) high angular annular dark field (HAADF), and energy dispersive X-ray spectroscopy (EDX)

SEM and TEM images were collected using an Hitachi SU-70 and FEI Tecnai Osiris respectively. For SEM analysis, a thin layer of powder was adhered to double-sided carbon tape and then examined using a 15 kV acceleration voltage. For TEM, 1 mg powder was dispersed in 10 ml of ethanol or deionized water using ultrasonication and then deposited dropwise to a holey carbon coated gold grid. TEM images were acquired using an acceleration of 200 kV. Multiple spots were examined on all samples to ensure sample uniformity. EDX elemental analysis and mapping was used in TEM-HAADF mode to identify and differentiate between copper and iron in samples.

Atomic force microscopy (AFM)

AFM images were collected on a Bruker Dimension Fastscan using a ScanAsyst Air probe tips. Samples were dispersed in ethanol and then drop cast on silicon wafer. Multiple regions of the sample were scanned to ensure sample uniformity.

X-ray diffraction (XRD)

XRD spectra were collected on a Rigaku SmartLab X-ray diffractometer using Cu Kα radiation (λ = 1.5418 Å) with a rotating anode source, operated at 45 kV and 200 mA. Powder samples were measured on glass slides and lattice constants and crystallite sizes were obtained using PDXL 2 Rigaku data analysis software. PDF card 00-001-1053 was used as a reference for hematite.

X-ray photoelectron spectroscopy (XPS)

The XPS spectra were collected using monochromatic 1486.7 eV Al Kα X-ray source on PHI VersaProbe II X-ray Photoelectron Spectrometer with a 0.47 eV system resolution. The energy scale has been calibrated using Cu 2p$^{3/2}$ (932.67 eV) and Au 4f7/2 (84.00 eV) peaks on a clean copper plate and a clean gold foil. The resolution of the instrument is approximately 0.5 eV.

Attenuated total reflectance Fourier transformed infrared spectroscopy (ATR-FTIR)

Powder samples were measured using a Thermo Nicolet 6700 FTIR with diamond ATR attachment and KBr beam splitter. Transmission measurements were conducted at room temperature using a deuterated triglycine sulfate (DTGS) detector. Plots shown are the average of 32 scans collected over the range of 500–4000 cm^{-1}. An additional 8 scans were acquired as background before loading each sample.

Brunau–Emmet–Teller (BET)-N$_2$ physisorption

Surface area measurements were made on hematite powder samples using a Quantachrome autosorb. Adsorption–desorption isotherms were constructed using an 11 point Brunauer, Emmett and Teller (BET) measurements protocol with N$_2$ as the adsorbate. Typically 50–100 mg of sample was used and outgassed at 200 °C for 3–6 hours. Measurements of each sample were performed in triplicate and their average and standard deviation calculated.

H$_2$-Temperature programmed reduction (H$_2$-TPR) and reverse water gas shift (RWGS)-temperature programmed reaction (TPR)

H$_2$-TPR and RWGS-TPR were performed on powder samples using a flow reactor set up. Mass flow controllers were used to control gas flow rates and k-type thermocouples were used to control temperature. For TPR, 30–50 mg of iron oxide (30 mg for nanowires and nanosheets, 50 mg for nanoparticles) was loaded into a straight tube quartz reactor with a rough silica bed and controllably heated from 100 °C–400 °C at 10 °C min^{-1}. Over this period, gas was flowed over the sample at a rate of 100 ml min^{-1}; the composition of the feed gas was 10% H$_2$ and 90% Ar. The outlet gas composition was measured using an SRS RGA 100 Mass Spectrometer. In the case of iron oxide nanoparticles, 50 mg was used, because the signal to noise intensity suffered at lower mass loadings. Due to sample constraints, 50 mg could not be used for the nanowires or nanosheets.

RWGS-TPRs were performed in the same set up used for H$_2$-TPR. 50 mg of catalyst of each sample was loaded into a straight tube quartz reactor and heated typically from 100–900 °C. The gas flow rate was 100 ml min^{-1} and the inlet feed composition 20% H$_2$, 20% CO$_2$, and 60% Ar.

To quantify CO$_2$ conversion, the outlet gas composition was compared to measurements of the pre-reaction steady state CO$_2$ mass spectrometer signal. Using the equation below, CO$_2$ conversion was calculated at each point. Measurements were taken approximately every 3 seconds. No change in Argon signal was observed indicating that the partial pressure in the chamber remained constant.

$$\%CO_2 \text{ conversion} = \left(1 - \frac{\text{Measured } CO_2 \text{ signal}}{\text{Pre-reaction } CO_2 \text{ signal}}\right) \times 100$$

Molecular modelling

We used the Vienna *ab initio* simulation package (VASP)[33–36] for all periodic boundary calculations. The projector augmented plane wave (PAW) method[37,38] together with the PBE exchange–correlation functional[39] were employed to describe the electron-ion interactions. The PBE+U method was used, following Dudarev's approach[40] to add on-site potentials to the d electrons of transition metals to describe properly the electronic states of transition metal oxides. $U_{\text{eff}} = U - J$ parameters of 4.0 and 7.5 eV were used for Fe$_2$O$_3$ and CuO to reproduce the experimental band gaps of bulk metal oxides. A cutoff of 450 eV was chosen for the plane wave basis set in all calculations. A 3 × 3 × 3 Monkhorst–Pack type k-point grid was chosen for the optimization of bulk Fe$_2$O$_3$, while a 7 × 7 × 7 Monkhorst–Pack type k-point grid was chosen for the optimization of bulk CuO. A Gaussian smearing (σ) of 0.1 eV was used. The energy convergence criterion was set to be 10^{-4} eV per unit cell and the force convergence criterion of 0.01 eV Å^{-1} was used for all structure optimization. Supercell with the dimension of 9.38 Å × 6.86 Å × 25.26 Å with OH termination were used to model the CuO (002) surface. Supercells with the dimension of 8.76 Å × 25.12 Å × 13.84 Å and 36.69 Å × 5.06 Å × 24.51 Å were used to model the Fe$_2$O$_3$ (110) and (104) surfaces, respectively. The bottom 2 layers of Fe and bottom layer of O atoms were fixed at the bulk position during geometry optimization. The binding energy (BE) was calculated as BE = $E_{\text{total}} - E_{\text{ads}} - E_{\text{surf}}$, where E_{total} is the total energy of the absorbed system, E_{ads} is the energy of the adsorbate in vaccum and E_{surf} is the energy of the optimized bare surface. A 3 × 3 × 1 Monkhorst–Pack k-point mesh was used for all slab calculations. For the calculation of small adsorbate molecules, a supercell of 15 Å × 15 Å × 15 Å and a 1 × 1 × 1 Monkhorst–Pack k-point mesh were used.

Results and discussion

Structure

The structure of each material was examined using SEM and TEM, as shown in Fig. 1 and ESI (Fig. S1 and S2†). Iron hydroxide nanosheets were grown using copper oxide nanosheets as a hard template. Copper oxide is a non-hazardous material, studied in previous works.[31] CuO nanosheets are stable in various solvents such as water, ethanol, and toluene for short periods of time (*e.g.* days) with high activity and an amenable shape for synthesizing other 2D materials through templating. Ferrous sulfate was used as a precursor for iron hydroxide nanosheet growth because it is a mild reducing agent while CuO is a mild oxidizing agent. We assume that growth occurs *via* a redox mechanism on the surface of the CuO nanosheets. Fe^{2+} ions are attracted to the hydroxyl rich surface of the metal oxide template. Upon heating, the Fe ions participate under mild redox reaction conditions, forming a 2D Fe^{3+} hydroxide, analogous to the chemistry of soil.[41]

To explore the validity of the proposed 2D Fe^{3+} hydroxide formation mechanism, we used DFT calculations to determine the binding energy of ferrous hydroxide to the surface of the copper oxide, as shown in Fig. 2. Previous experimental data on CuO nanosheets was used to inform the design of the computational models.[31] Lattice parameters were extracted from XRD spectra and the facet (002) was selected for adsorption, based on its prominent relative XRD peak intensity. The model facet (002) was terminated by hydroxyl groups, because the synthesis was performed under aqueous conditions. The resulting models provided band gaps in agreement with experimental UV-visible spectroscopy results.[31] Ferrous hydroxide was selected as the adsorbate since ferrous sulfate was the experimental precursor, which stably coordinates with two water molecules. We find that ferrous hydroxide favorably binds (BE = −0.7 eV) to the hydroxyl terminated (002) surface of the simulated CuO nanosheet. During the binding process, a coordinated water molecule is displaced and the iron ion becomes coordinated to three surface oxygen species of CuO. Direct attempts to oxidize Fe^{2+} by reducing the lattice Cu^{2+} to
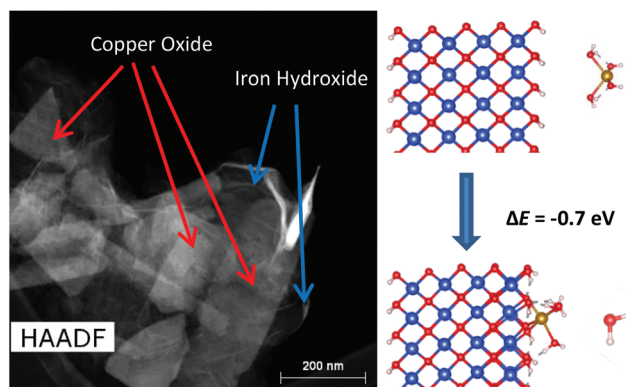

Fig. 2 TEM HAADF image of copper oxide-iron hydroxide nanosheets (post-synthesis, pre-ammonium hydroxide wash) accompanied by DFT calculations showing favorable binding of $Fe(OH)^{2-} \cdot 2H_2O$ to the surface of copper oxide. The atoms' color corresponds to its type, blue: Cu, red: O, Brown: Fe, white: H. The calculations were made on the (002) facet of a hydroxyl terminated thin copper oxide sheet.

Cu^+ were unsuccessful, suggesting that other species (*e.g.*, surface hydroxyl groups, or dissolved oxygen) may play a crucial role in the formation of ferric hydroxide nanosheets. Further spectroscopic evidence supports formation of ferric hydroxide nanosheets (Composition section), rather than formation of ferrous hydroxide nanosheets.

SEM and TEM images of the ferric hydroxide nanosheets (Fig. S1b and d†), show that the sheets are polycrystalline with length and width of approximately 1–1.5 μm. Note that these dimensions are larger than the CuO nanosheets, which suggests that either multiple CuO nanosheets participate in the growth of a single iron hydroxide nanosheet, or that the template is not necessary for all stages of growth. For example, if the synthesis follows a nucleation, elongation and termination process, it is possible that CuO nanosheets are only necessary for nucleation and part of the elongation process while further elongation may occur beyond the sheet. CuO nanowires, nanopowder and bulk were also attempted to be used as a template. Interestingly, besides the CuO nanosheets, only the CuO nanowires were effective at templating iron hydroxide nanosheets likely due to the presence of highly active edge sites as in CuO nanosheets. Without CuO nanosheets, or nanowires, iron hydroxide nanosheet growth was not observed indicating that the template structures are essential at least for the initiation step.

After synthesis, ammonium hydroxide was used to remove the CuO nanosheets. Unlike a strong acid, which would solubilize both the copper oxide and iron hydroxide, ammonium hydroxide is selective only for copper. Prior to ammonium hydroxide treatment, CuO nanosheets were found in ferric hydroxide nanosheet samples. TEM-HAADF images are shown in Fig. 2; EDX elemental mapping was used to clearly differentiate the iron containing nanosheets from the copper oxide nanosheets, as shown in Fig. S1e and f.† No CuO nanosheets were found in TEM images after ammonium hydroxide, such as those depicted in Fig. 1d. In the subsequent sections, we
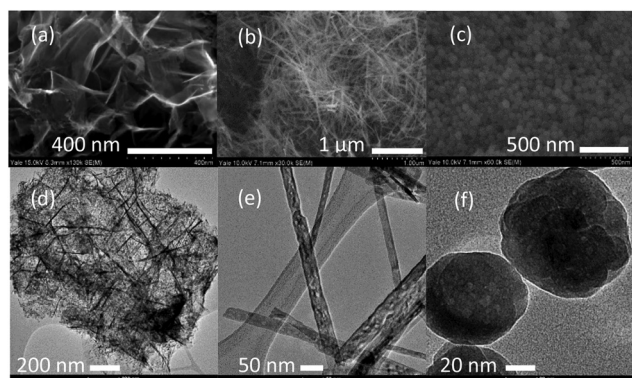
Fig. 1 SEM (a–c) and TEM (d–f) of hematite nanosheets (a, d), nanowires (b, d), and nanoparticles (c, f).

discuss results of other characterization techniques, including XRD, FTIR and XPS, which further demonstrate effective removal of the CuO template.

Goethite (α-FeOOH) nanowires were grown in aqueous phase basic solution without using a template and under inert gas conditions. SEM and TEM images of the nanowires are shown in Fig. S1a and c.† Compared to the nanosheets, they appear to be more crystalline with a diameter of approximately 20–37 nm. Though reproducible, we found that the synthesis conditions for goethite nanowires must be carefully controlled. Heating above 50 °C during synthesis induces formation of magnetite nanoparticles according to the Schikorr reaction, resulting in a suppression of nanowire growth, Fig. S3.† [42] Additionally, in the absence of N_2 bubbling no nanowires were formed, only nanoparticles. In previous work, dissolved oxygen has been proposed as the oxidizer, however we found that goethite nanowire formation only occurs with N_2 bubbling, i.e. in the absence of oxygen. Therefore, we posit that goethite nanowire are formed through an alternative pathway involving hydroxyl ions.

Thermal oxidation was used to convert ferric hydroxide nanosheets and goethite nanowires into hematite nanosheets and nanowires. Ferric hydroxide nanosheets were heated in air to 400 °C for 30 min for oxidation to hematite nanosheets while goethite nanowires were heated to 400 °C for 15 min for oxidation to hematite nanowires. SEM and TEM images of the heated hematite nanosheets and hematite nanowires are presented in Fig. 1a, b, d, and e. These images reveal only minor structural differences between the unheated and heated iron oxide samples. AFM was subsequently used to find the thickness of these materials, Fig. S4.† Through this method, hematite nanosheets were found to have a thickness of 4–7 nm and hematite nanowires were found to have a diameter of 20 nm. For hematite nanowires, this agrees well with diameters measured using TEM imaging. Additionally, the gradual height increase observed in the nanowires compared to the abrupt edge step of the nanosheets shows that the edges of the nanowires are smooth while the nanosheets are rough. Roughness can also be seen over the face of the nanosheets.

Hematite nanoparticles were synthesized using a slightly altered version of a previously established wet chemical protocol.[32] SEM and TEM images of the sample can be found in Fig. 1c and f. The particles appear more crystalline than the nanosheets or nanowires and were observed to vary in diameter between 50 nm and 67 nm.

Additional information on the structure of these materials was obtained through BET-N_2 physisorption. Unsurprisingly, the nanosheets have the highest surface area with a value of 139.0($\pm$5.7) m^2 g^{-1} followed by the nanowires with a value of 39.1($\pm$0.5) m^2 g^{-1}, and finally by the nanoparticles with a surface area of 18.8($\pm$1.9) m^2 g^{-1}. Additionally, surface area can be used to obtain the average value for the nanodimension of a sample such as thickness of a nanosheet[31] or diameter of a nanoparticle.[43] The equation for each of these has been added to the ESI† as well as a derivation for obtaining the diameter of a nanowire based on its surface area and density. The calcu-

**Table 1** Nano-size derived from various techniques

Sample	From TEM/AFM (nm)	From BET (nm)	From XRD (nm)
Nanosheets	4–7	2.62–2.83	4.3–6.5
Nanowires	20–37	19.1–19.6	8.3–9.5
Nanoparticles	50–67	54.6–67.0	37.8–39.8

lated average thickness of the nanosheets is 2.73 nm and the calculated average diameter for nanowires and nanoparticles were 19.4 nm and 60.8 nm, respectively. A comparison between diameter and thickness values obtained via imaging, surface area, and X-ray diffraction (crystallite size) is presented in Table 1. Based on SEM, TEM and AFM images it would appear that the surface area predictions slightly underestimate the thickness of the nanosheets and the diameter of the nanowires. Underestimations such as these could be due to high surface roughness. TEM images of the hematite nanosheets and nanowires reveal a large number of defects in these structures supporting this hypothesis.

Composition

XRD, FTIR, and XPS were used to determine the composition of each of these materials. XRD spectra, Fig. 3, of nanosheets and nanowires before heating matched literature sources of 6-line ferrihydrite and goethite, respectively. These are both semi-stable forms of iron hydroxide phases composed of a mixture of Fe^{3+}. The 6-line ferrihydrite is not very crystalline, characterized by broad weak peeks that are difficult to assign. Importantly, no CuO peaks were detected in nanosheet samples washed with ammonium hydroxide. This indicates that the washing treatment was effective for removing the hard template.

Though some iron hydroxides, such as ferrihydrites and green-rust, have a tendency to oxidize in air, many researchers have characterized iron hydroxides for their ability to adsorb arsenic[44,45] and chromate,[46] as well as for their ferromagnetic properties.[10] In this work, the iron hydroxides synthesized
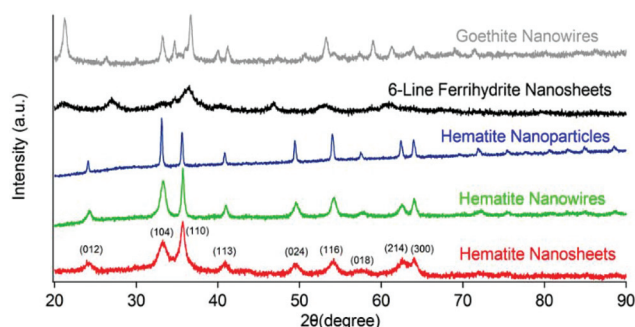
Fig. 3 XRD spectra of iron oxide and hydroxide nanostructures. From top to bottom these structures were identified as goethite nanowires (grey), 6-line ferrihydrite nanosheets (black), hematite nanoparticles (blue), hematite nanowires (green), and hematite nanosheets (red). Peaks are labelled with their corresponding faces for hematite.

were thermally oxidized into nanowires and nanosheets of hematite because of its enhanced stability. The XRD spectra of these thermally oxidized nanosheets and nanowires are also presented in Fig. 3. Compared to the hematite nanoparticles, the nanosheets and nanowires have a higher relative intensity of the (110) peak to the (104). From TEM images (Fig. 1), we observe that neither of these materials are single crystalline, however the relative intensities of these peaks suggest increased expression of the (110) facet in the nanowires and nanosheets compared to the nanoparticles, which have a higher relative intensity of the peak associated with the (104) facet. We will discuss the potential impact this may have on catalysis in the subsequent section.

In nanomaterials, peak broadening often occurs in XRD spectra and can be used to calculate crystallite size using the Scherer equation. Here, the software package PDXL2 was used to calculate crystallite sizes of each material. 6-Line ferrihydrite nanosheets and goethite nanowires were found to have smaller crystallite sizes of 1.67 nm and 6.5 nm, both smaller than their oxidized counter parts suggesting that crystallinity increases with annealing. For hematite nanosheets, nanowires, and nanoparticles the average crystallite size was found to be 5.4 nm, 8.9 nm, and 38.8 nm, respectively. Looking at Table 1, we find that the crystallite size is consistent with AFM measurement of the thickness of the nanosheets. For nanowires, the value is approximately half that of the measured diameter indicating that these structures are polycrystalline, as observed by TEM (Fig. 1). The crystallite size of the nanoparticles is larger than that of the nanowires or nanosheets, though is smaller than the diameter observed for these particles in TEM or calculated from surface area measurements. This would imply that while the nanoparticles are more crystalline than the nanowires or nanosheets, they are still polycrystalline. While there are many factors that may lead to peak broadening, such as inhomogeneity and lattice strain, we believe that nanoscale crystallite size is the main contributor. FTIR-ATR as well as XPS data supports the claim that the hematite samples are homogenous and do not contain unreacted hydroxides. Additionally, we calculated no significant lattice strain in any of these materials using the PDXL2 software package.

Absorbance FTIR-ATR data obtained for all powder samples is shown in Fig. S5.† The hematite nanoparticles, nanowires, and nanosheets all share similar features 428 cm^{-1}, 515 cm^{-1}, and a shoulder region typical of the Fe–O vibration in hematite.[47,48] While the peak at 428 cm^{-1} is well aligned for all three of these samples, the second peak is shifted slightly from 515 cm^{-1} for the nanoparticles and nanowires to 522 cm^{-1} for the nanosheets. Additionally, the shoulder region is also shifted. These shifts in phonon energies can be attributed to difference in crystallite size, aspect ratio, as well as differences in the expression of specific crystal facets, as shown by XRD.[49] For the hematite nanoparticles there is small, broad hydroxyl peak around 3300 cm^{-1}. This is expected since the nanoparticle powder is the only hematite sample that was not annealed. The FTIR spectra of unheated nano-

wires corresponds very well with goethite based on previous studies.[42] The lack of distinct features in the FTIR spectrum of unheated nanosheets sample makes it difficult to classify and suggests that the material is an iron hydroxide such as 6-line ferrihydrite, as suggested by the XRD data. The lack of goethite peaks in the hematite nanowire spectra also suggests that the annealing process effectively converted all of the goethite into hematite.

To further characterize the surface of these materials XPS was performed; Fig. 4 contains Fe 2p (a) and O 1s (b) data for all samples. Little variation was found between the samples on Fe 2p edge. All display peaks at 710.7 and 724.0 eV corresponding to Fe $2p^{3/2}$ and Fe $2p^{1/2}$ respectively and broad peaks at approximately 718 and 733 eV are Fe^{3+} satellite peaks.[50–53] Data from the Fe 2p edge would seem to suggest that the surface of all samples contain iron in the +3 oxidation state. This result is not surprising since all samples were stored at room temperature in air and Fe$_2$O$_3$ is the most stable form of iron oxide under those conditions. Though typically thought of as a surface technique, in this case the penetration depth of XPS (~10 nm) exceeds that of the nanosheet thickness (~5 nm) and therefore can be used as evidence that the iron hydroxide nanosheets are indeed ferric hydroxide and not ferrous hydroxide. This supports the argument made previously that redox occurs at the surface of CuO nanosheets during synthesis converting Fe^{2+} to Fe^{3+}.

At the O 1s edge there is significant difference between the samples; Fig. S6† shows the O 1s deconvolution data for the hematite nanoparticles, 6-line ferrihydrite nanosheets, and goethite nanowires. Firstly, all sample share a peak at approximately 529.7 eV corresponding to oxygen in iron oxides or iron hydroxides. However, this is where the similarities between the spectra end. For the hematite nanoparticle sample, the broad
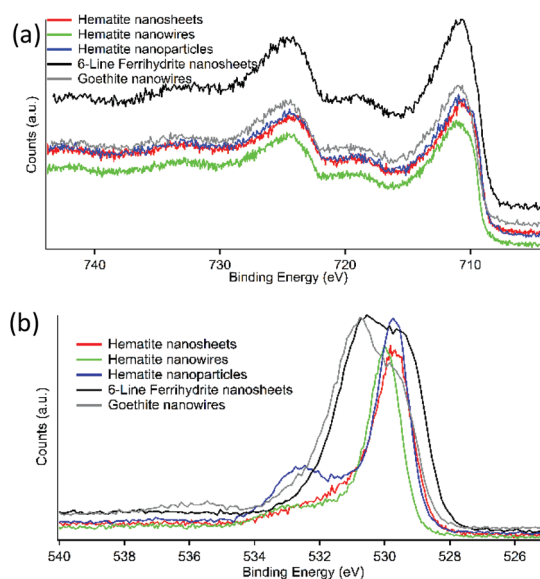

Fig. 4 XPS Fe 2p (a) and O 1s (b) spectra of iron oxide and hydroxide nanostructures.

peak at approximately 532.3 eV corresponds to oxygen that is part of a hydroxyl group, for example in adsorbed water.[54] We observe here that the hematite nanoparticles have more hydroxyl groups bound to their surface than the hematite nanosheets or nanowires. This observation is consistent with the FTIR data previously discussed. This heightened surface hydroxylation is due to differences in synthesis (*e.g.* annealing), or material property differences such as differences in crystal facet expression. In the following section, we will show using DFT calculations that the (104) facet is less stable, which may be a cause of this hydroxylation. The secondary oxygen peak in the goethite and the 6-line ferrihydrite is shifted towards lower binding energy, 530.6 eV, and is even greater in magnitude than the oxide peak. This suggests that the hydroxyl groups are within the structure of the material, corroborating the FTIR and XRD data, that these are indeed iron hydroxides.[54] This data further supports the claim that the hematite nanosheet and nanowire samples do not contain unreacted hydroxides.

Optical properties

The band gaps of the samples were measured using UV-visible spectroscopy and the results displayed in Fig. 5 and Table 2. Absorbance intensity was measured on dispersed solutions of each powder over a range of 400–1000 nm, and then converted to a Tauc plot using a transformation that is well established in the literature.[31] For this transformation, we tested various exponential values corresponding with direct and indirect,
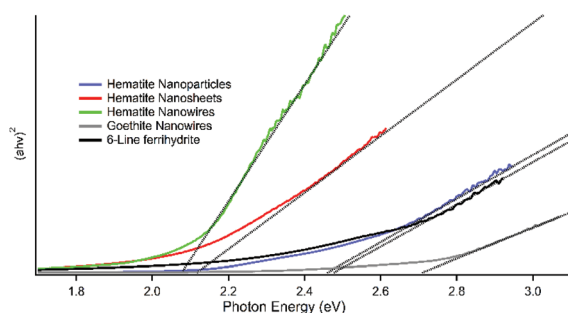
Fig. 5 Tauc plots obtained from UV-Vis data collected on iron oxide and hydroxide nanostructures. The dotted lines are extrapolations of the linear region of each curve down to the *x*-axis used to compute each structure's respective band gap.

Table 2 Mean values for the band gap of each iron hydroxide or oxide structure

Sample	Band gap (eV)
Hematite nanosheets	2.12
Hematite nanowires	2.08
Hematite nanoparticles	2.46[a]
Goethite nanowires	2.70
6-Line ferrihydrite nanosheets	2.47[a]

[a] Samples that exhibited sub-bandgap absorption

allowed and forbidden transitions and found that these materials displayed an allowed direct band transition. This is contrary to some literature reports on bulk hematite, but is in line with more recent reports for nanostructured hematite.[55] The band gap of each material was found by extrapolation of the linear region of each trace down to the abscissa indicating the energy of the incoming photon. We observed very similar band gap values for the hematite nanosheets and nanowires, 2.12 eV and 2.08 eV respectively. These values were similar those typically reported in the literature for bulk and nano-hematite.[56] Hematite nanoparticles were found to have a band gap of 2.46 eV, much higher than the nanosheets, nanowires, and other values previously reported for nanoparticles. It is unlikely that this difference is due to particle size since previous studies have demonstrated that this does not have a large impact on the band gap of hematite.[56] Another explanation is that nano-dimension and crystal facet exposure play a role. Other sources have shown absorption difference based on crystal facet in thin films and platelets.[57] Difference in nano-dimension and crystal facet exposure may also be having a less direct impact on band gap by affecting surface hydroxylation. We have shown through XPS (Fig. 4) and FTIR (Fig. S6†) that the hematite nanoparticles contain more hydroxyl groups than the nanosheets or nanowires. In other systems, such as CuO nanosheets, surface oxygen defects can significantly change the band gap by as much as 0.4 eV.[31] Furthermore, the band gap of the computational CuO model used in this report (Fig. 2) is hydroxylated, which increased the calculated band gap from 1.2 to 1.7 eV.

A closer inspection of the hematite nanoparticle UV-Vis spectra reveals a significant amount of light absorption below the band gap energy. This sub-band gap absorption has not been reported for hematite, but researchers have observed this phenomenon in other materials such as $InVO_4$.[58] In this work, extrapolation of the linear pre-band gap region between 2.2 and 2.6 eV yields an intersection with the *x*-axis at 2.12 eV, surprisingly similar to the other samples and the reported band gap of hematite. This seems to suggest that the difference in band gap may be due to either multiple transitions within the same material.

Further insights into this come from looking at the spectra of the 6-line ferrihydrite nanosheets. Similar to the nanoparticles we find a band gap of 2.45 eV with a strong sub-band gap absorption region, which if extrapolated, yields a band gap of 2.12 eV. This, taken in conjunction with the previous data and discussion on surface hydroxylation, seems to suggest that hydroxyl group significantly affect the optical properties of iron oxide and hydroxide.

Finally, we find that the goethite nanowires have a band gap of 2.70 eV, higher than previously reported values, which may be due to nanostructure.[59] Comparing the iron hydroxide samples to their iron oxide counterparts, we conclude that the optical properties of iron hydroxides are more tunable than iron oxides and that differences in the optical properties of iron oxides may be due to surface hydroxyl species. Understanding these differences and finding correlations to

catalytic properties is an important step towards aiding molecular modelling of complicated systems and finding good descriptors for catalytic behaviour.

Catalytic properties

Reverse water gas shift temperature programmed reactions (RWGS-TPR) were conducted on hematite nanoparticles, nanowires, and nanosheets. CO_2 conversion as a function of temperature is plotted in Fig. 6. 50 mg of each material was used for the study and heated in a 20% CO_2, 20% H_2 with Ar as the inert carrier gas. The stoichiometry of the RWGS reaction, shown in eqn (1), allows us to use CO_2 conversion as a probe of the reaction.

On a pure mass basis, the iron oxide nanosheets are superior to the nanoparticles or nanowires for converting CO_2 to CO below 510 °C, peaking at approximately 30% conversion. Above 510 °C the conversion of CO_2 to CO over the nanosheets plateaus and then decreases while the conversion over the nanowires increases up to 55% at 850 °C. Fig. S7† shows a complete mass spectrum of all species measured. Though this mass spectrometer allows for a high rate of collection (every 3 seconds), it only allows for 10 m/z channels to be probed at a time. However, since higher molecular weight products tend to fragment due to the large energy used to ionize the gases, they may be detected at lower m/z channels. Despite probing other channels, such as those associated with methane, methanol, formaldehyde, ethane and other higher molecular weight species, no products besides CO and H_2O were detected at this $H_2 : CO_2$ feed ratio. At larger feed ratios however, coking and formation of larger chain carbon species was found to occur (data not shown). This is likely due to Fischer Tropsch side reactions. Iron and its oxides have been long studied for their ability to convert CO and H_2 to longer chain olefins at elevated temperatures.[60]

Taking surface area into account, Fig. S8,† we find that the turn over frequency (TOF) for the nanowires exceeds that of the nanosheets at all temperatures. At 510 °C the TOF of the nanosheets is 0.035 mmol m^{-2} min^{-1} while the nanowires have a TOF of 0.111 mmol m^{-2} min^{-1}. At 750 °C the TOF of the nanowires rises to 0.210 mmol m^{-2} min^{-1} while the TOF of the nanosheets drops to near zero due to restructuring and

loss of surface area. We find the nanoparticles to be unreactive at low temperatures but begin to become active above 600 °C. At 750 °C their CO_2 conversion is 9% corresponding to a TOF 0.083 mmol m^{-2} min^{-1}. The data on turn over frequency for these samples indicates that on a pure site basis the nanowires are the most reactive regardless of reaction temperature. At low temperatures, the sites of the nanosheets seem superior to the nanoparticles, however at higher temperatures the reactivity of the nanosheets falls off while the reactivity of the nanoparticles seems to increase. We assume that the drop off in nanosheet reactivity is due to catalyst instability, since at high temperatures nanomaterials are known to lose structure and sinter.

There are a number of reasons why the nanosheets may be less stable than the nanowires, and why the nanoparticles are less reactive. In previous sections, we discussed how nanosheets have higher surface roughness and more defects than either of the other two structures, while the nanoparticles have a higher proportion of crystal facet (104) exposed than the nanowires or nanosheets, which display increased (110) facet exposure. Another possibility is that the nanostructure itself plays a critical role. In other materials thickness and shape create highly active sites due to contributions from curvature and edge states.[61]

We posit that the first step for the RWGS reaction over hematite is H_2 binding to the surface and reducing the material to magnetite. Under oxidizing conditions hematite is the most stable form of iron oxide, however under reaction conditions the samples are exposed to a highly reducing atmosphere due to elevated presence of H_2 gas. Additionally, there are no reports of hematite being able to reduce CO_2 to CO *via* RWGS, however there are reports of magnetite being able to.[62]

To gain further insight into this system, H_2 temperature programmed reduction (H₂-TPR) was performed and compared with H_2 binding energy calculations. In Fig. 7a, the experimental H_2 consumption is plotted as a function of temperature for hematite nanosheet, nanowire, and nanoparticle samples. For the nanosheets and nanowires, two peaks are visible in each. The first sharp peak occurs at 225 °C for the nanosheets and 325 °C for the nanowires, while the second broad peak coincides in the region from 400 °C to 600 °C. For the nanoparticles, there is only a broad peak at 550 °C with a shoulder at 450 °C, indicating at least two overlapping peaks.

These peaks in H_2 consumption correspond to H_2 adsorption and reduction of the catalyst. We suggest that the first peaks in these plots are due to the reduction of hematite to magnetite, as follows:

$$Fe_2O_{3(s)} + H_{2(g)} \rightarrow Fe_3O_{4(s)} + H_2O_{(g)}. \tag{2}$$
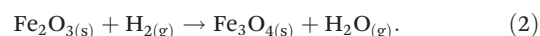
XRD was performed on iron oxide nanosheet samples after heating to 250 °C, 500 °C, and 700 °C in 10% H_2, Fig. S9.† Before heating the iron oxide nanosheets were confirmed as hematite using a variety of characterization techniques as discussed earlier. After heating to 250 °C in 10% H_2, past the first H_2 TPR peak, the XRD spectra correspond well with that of
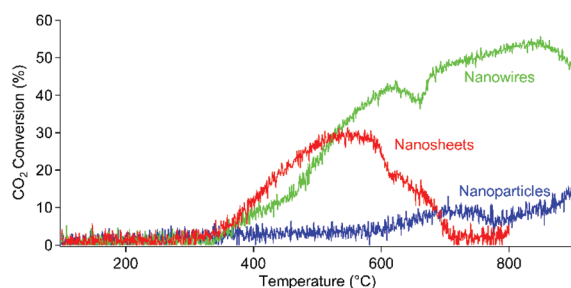

Fig. 6 On-line mass spectrometry measurements during RWGS-TPR of hematite nanosheets, nanowires, and nanoparticles. %CO_2 conversion was computed using differences in the m/z = 44 channel as a function of temperature.
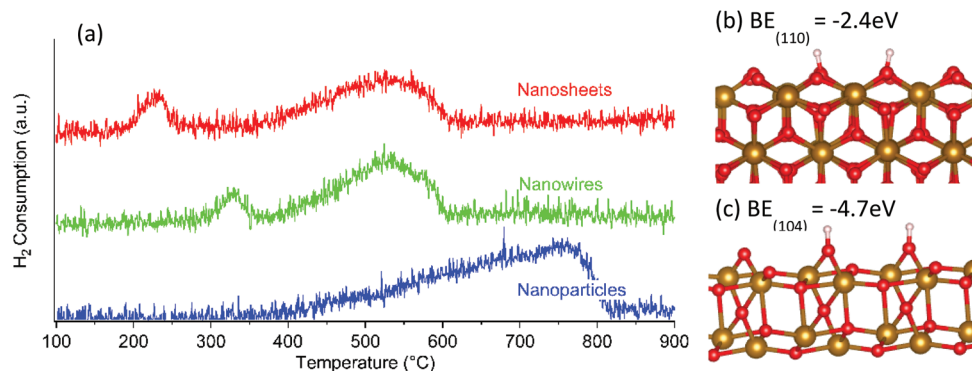
Fig. 7 H_2-TPR mass spectrometry data (m/z = 2) for hematite nanoparticles, nanowires, and nanosheets (a), accompanied by DFT binding energy calculations on hematite (110) (b) and (104) (c) surfaces. Here, Fe is in brown, oxygen is in red, and hydrogen is in white.

magnetite, Fe_3O_4. SEM images were also taken of the samples after reduction at 250 °C, Fig. S9b,† and though significant defects are visible, the nanosheets more or less maintain their structure making this a possible route for producing high surface area polycrystalline magnetite nanosheets. XRD spectra of nanosheets heated under similar conditions to 500 °C, representative reaction conditions, reveals a mixture of Fe_3O_4 and Fe. Further heating to 700 °C reveals a decrease in intensity of peaks associated with Fe_3O_4, leaving solely peaks associated with Fe. This seems to indicate that the second broad TPR peak in the nanosheets and nanowire samples corresponds to the reduction of magnetite to iron metal, eqn (3).

$$Fe_3O_{4(s)} + 4H_{2(g)} \rightarrow 3Fe_{(s)} + 4H_2O_{(g)}. \tag{3}$$
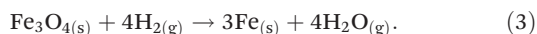
Since the location of these peaks is dependent on the catalyst used we may say that it is a quantitative measure of the materials stability and reactivity. That is, since the H_2 consumption peak for hematite nanosheets is at the lowest temperature, 225 °C, we would expect them to be the most reactive, but least stable. The opposite may be said of the nanoparticles which do not show any reactivity with H_2 below 400 °C. In the middle of these two we find the nanowires with an H_2 consumption peak around 325 °C.

One explanation for differences in reactivity between the nanoparticles and the other two structures is differences in exposed crystal facet, previously shown in Fig. 3. DFT calculations were performed to model the binding of H_2 on hematite (110) and (104) surfaces, Fig. 7b and c. Several binding configurations were attempted and their structures were allowed to relax. In the lowest energy configuration for each face, it was found that hydrogen atoms preferred to rest on oxygen sites while electron density was transferred to the adjacent iron sites. This results in reduction of these iron atoms from Fe^{3+} to Fe^{2+} consistent with eqn (3). We find that H_2 adsorption to (104) facet has a lower binding energy, −4.7 eV, than does the (110), −2.4 eV, meaning that one would expect structures with more prominent (104) facet exposure to be more reactive during H_2-TPR than those with greater (110) exposure. However, experimentally we observe the opposite.

The hematite nanosheets and nanowires, which react with H_2 at lower temperatures, have XRD spectra with higher (110) exposure relative to (104) compared to the nanoparticles. This would indicate then that exposed crystal facet is not the only guiding factor in reactivity, but rather the nanostructure itself plays a critical role. This is reinforced by the fact that the relative intensities of XRD peaks in the nanowires and nanosheets are similar, but these structures too exhibit differences in reactivity.

The broad peak in the region from 400 °C to 600 °C for the nanowires and nanosheets aligns very well with the peak for CO_2 conversion seen in the RWGS-TPR experiments. Since these broad H_2 TPR peaks in nanosheets and nanowires are similar in location and shape to each other and to the peaks in the CO_2 conversion plots, it would suggest that the mechanism of H_2 oxidation over both of these materials is similar. Furthermore, it suggests that the conversion of CO_2 to CO over these materials in this temperature regime is gated by H_2 adsorption and/or reduction of the catalyst, i.e. from Fe_3O_4 to Fe, eqn (4). A similar argument can be made for the nanoparticles over the range of 600 °C to 775 °C.

At higher temperatures, above 600 °C for the nanowires and nanosheets and above 800 °C for the nanoparticles, the CO_2 conversion and H_2 consumption data diverge. In the nanowires, H_2 consumption during TPR drops to zero above 600 °C, while for RWGS-TPR CO_2 conversion only briefly dips from 600 °C to 650 °C and then steadily rises until 850 °C, where conversion finally begins to fall. The nanosheets also show a precipitous drop in H_2 consumption above 600 °C during TPR, however the same material shows a wide shoulder region in CO_2 conversion from 600 °C to 700 °C during RWGS-TPR. In the case of the nanoparticles, H_2 consumption falls off sharply above 775 °C, while only a brief dip is observed for CO_2 conversion during RWGS-TPR. This would suggest that at higher temperatures the catalysts performance for CO_2 conversion is strongly dependent on its ability to be re-oxidized by CO_2, eqn (4).

$$3Fe_{(s)} + 4CO_{2(g)} \rightarrow 4CO_{(g)} + Fe_3O_{4(s)}. \tag{4}$$
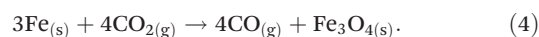
To gain further insights into the structural stability of these materials, SEM images were acquired after reaction. Fig. S10a

and b† contain images of iron oxide nanosheets and nanowires heated to 500 °C in 20% CO_2, 20% H_2, 60% Ar for 15 minutes. After heating, the nanostructure of the nanosheet sample seems to have completely changed while the nanowires sample seems to have retained some semblance of structure. This evidences the claim that the nanowires are more stable than the nanosheets and that there is a balance between high temperature stability and high reactivity. It also suggests that catalytic activity losses are expected to occur over similar time scales under these conditions. An XRD pattern of the nanosheet sample was also collected after this reaction and showed that the composition had indeed changed to magnetite, Fig. S10c.†

Finally, we should consider how the optical properties of these materials correlate with their catalytic properties. The hematite nanoparticles which had the largest band gap were the least reactive while the nanosheets and nanowires had a smaller band gap and were more reactive at low temperatures. This link between optical and catalytic properties has been seen in other materials and may make band gap a good descriptor for catalytic activity in this system.[31,63]

Conclusions

We have introduced a novel technique for synthesizing iron oxide and hydroxide nanosheets as well as iron oxide nanowires, based on a hard template CuO substrate. DFT computations support a reaction mechanism based on binding of iron precursors binding to the copper oxide nanosheets surface through hydroxyl group coordination. The calculations suggest that the CuO nanosheet should also be useful as a hard template to grow other metal oxides.

We have characterized the structure, composition and optical properties of the resulting materials through a wide range of characterization techniques and we have demonstrated the utility (and drawbacks) of the resulting nanosheet materials for catalytic conversion of CO_2 into CO, *via* the RWGS reaction.

We found that hematite nanomaterials are reduced to magnetite, before the onset of the RWGS reaction. During the RWGS reaction, the catalyst is a mixture of magnetite and iron metal, with structural and composition stability found to be critical for high CO_2 conversion (*e.g.* nanowires). Stability and reactivity must be balanced to optimize CO_2 conversion. In particular, a decrease in catalytic activity is observed when too much of the nanomaterial converts into iron metal. Additionally, we found some correlation between band gap and activity. Materials with a lower band gap, such as the nanowires and nanosheets, exhibit higher reactivity at lower temperatures when compared to nanoparticles that have a higher band gap and exhibit no reactivity at low temperature. The reported findings are thus particularly valuable to the development of catalytic materials for CO_2/CO conversion, as in the RWGS system and the water–gas-shift reaction.

Conflicts of interest

There are no conflicts of interest to declare.

Acknowledgements

References

1 S. D. Tilley, M. Cornuz, K. Sivula and M. Grätzel, Light-Induced Water Splitting with Hematite: Improved Nanostructure and Iridium Oxide Catalysis, *Angew. Chem., Int. Ed.*, 2010, **122**, 6549–6552.

2 A. S. Madden, M. F. Hochella Jr. and T. P. Luxton, Insights for Size-Dependent Reactivity of Hematite Nanomineral Surfaces through Cu^{2+} Sorption, *Geochim. Cosmochim. Acta*, 2006, **70**, 4095–4104.

3 Z. Jinga, S. Wua, S. Zhanga and W. Huanga, Hydrothermal Fabrication of Various morphological a-Fe_2O_3 nanoparticles modified by surfactants, *Mater. Res. Bull.*, 2004, **39**, 2057–2064.

4 J. Lian, X. Duan, J. Ma, P. Peng, T. Kim and W. Zheng, Hematite (-Fe_2O_3) with Various Morphologies: Ionic Liquid-Assisted Synthesis, Formation Mechanism, and Properties, *ACS Nano*, 2009, **3**(11), 3749–3761.

5 C. Min, Y. Huang and L. Liu, High-yield synthesis and magnetic property of hematite nanorhombohedras through a facile solution route, *Mater. Lett.*, 2007, **61**, 4756–4758.

6 J. Liu, C. Liang, H. Zhang, S. Zhang and Z. Tian, Silicon-doped hematite nanosheets with superlattice structure, *Chem. Commun.*, 2011, **47**, 8040–8042.

7 J. Liu, C. Liang, G. Xu, Z. Tiana, G. Shao and L. Zhang, Ge-doped hematite nanosheets with tunable doping level, structure and improved photoelectrochemical performance, *Nano Energy*, 2013, **2**, 328–336.

8 J. Liu, Y. Y. Cai, Z. F. Tian, G. S. Ruan, Y. X. Ye, C. H. Liang and G. S. Shao, Highly oriented Ge-doped hematite

nanosheet arrays for photoelectrochemical water oxidation, *Nano Energy*, 2014, **9**, 282–290.

9 L. Wu, H. Yao, B. Hu and S. H. Yu, Unique Lamellar Sodium/Potassium Iron Oxide Nanosheets: Facile Microwave-Assisted Synthesis and Magnetic and Electrochemical Properties, *Chem. Mater.*, 2011, **23**(17), 3946–3952.

10 P. Chen, K. Xu, X. Li, Y. Guo, D. Zhou, J. Zhao, X. Wu, C. Wu and Y. Xiea, Ultrathin nanosheets of feroxyhyte: a new two dimensional material with robust ferromagnetic behavior, *Chem. Sci.*, 2014, **5**, 2251–2255.

11 J. Eastoe, M. J. Hollamby and L. Hudson, Recent advances in nanoparticle synthesis with reversed micelles, *Adv. Colloid Interface Sci.*, 2006, **128–130**, 5–15.

12 M. Zhang, M. Drechsler and A. H. E. Muller, Template-Controlled Synthesis of Wire-Like Cadmium Sulfide Nanoparticle Assemblies within Core-Shell Cylindrical Polymer Brushes, *Chem. Mater.*, 2004, **16**, 537–543.

13 Y. Song, R. M. Garcia, R. M. Dorin, H. Wang, Y. Qiu, E. N. Coker, W. A. Steen, J. E. Miller and J. A. Shelnutt, Synthesis of Platinum Nanowire Networks Using a Soft Template, *Nano Lett.*, 2007, **7**(12), 3650–3655.

14 J. S. Son, X. D. Wen, J. Joo, J. Chae, S. Baek, K. Park, J. H. Kim, K. An, J. H. Yu, S. G. Kwon, S. H. Choi, Z. Wang, Y. W. Kim, Y. Kuk, R. Hoffmann and T. Hyeon, Large-Scale Soft Colloidal Template Synthesis of 1.4 nm Thick CdSe Nanosheets, *Angew. Chem., Int. Ed.*, 2009, **121**, 6993–6996.

15 C. Xu, Y. Zeng, X. Rui, N. Xiao, J. Zhu, W. Zhang, J. Chen, W. Liu, H. Tan, H. H. Hng and Q. Yan, Controlled Soft-Template Synthesis of Ultrathin C@FeS Nanosheets with High-Li-Storage Performance, *ACS Nano*, 2012, **6**(6), 4713–4721.

16 N. Li, X. Wang, S. Derrouiche, G. L. Haller and L. D. Pfefferle, Role of Surface Cobalt Silicate in Single-Walled Carbon Nanotube Synthesis from Silica-Supported Cobalt Catalysts, *ACS Nano*, 2010, **4**(3), 1759–1767.

17 D. Ciuparu, R. F. Klie, Y. Zhu and L. D. Pfefferle, Synthesis of Pure Boron Single-Wall Nanotubes, *J. Phys. Chem. B*, 2004, **108**, 3967–3969.

18 T. L. Wade and J.-E. Wegrowe, Template synthesis of nanomaterials, *Eur. Phys. J.: Appl. Phys.*, 2005, **29**, 3–22.

19 Z. Zhang, F. Zuo and P. Feng, Hard template synthesis of crystalline mesoporous anatase TiO_2 for photocatalytic hydrogen evolution, *J. Mater. Chem.*, 2010, **20**, 2206–2212.

20 B. C. Satishkumar, A. Govindaraj, E. M. Vogl, L. Basumallick and C. N. R. Rao, Oxide nanotubes prepared using carbon nanotubes as templates, *J. Mater. Res.*, 1997, **12**(3), 604–606.

21 C. Li, M. Wei, D. G. Evans and X. Duan, Layered Double Hydroxide-based Nanomaterials as Highly Efficient Catalysts and Adsorbents, *Small*, 2014, **10**(22), 4469–4486.

22 Y. Chen, B. Song, X. Tang, L. Lu and J. Xue, Ultrasmall Fe_3O_4 Nanoparticle/MoS_2 Nanosheet Composites with Superior Performances for Lithium Ion Batteries, *Small*, 2014, **10**(8), 1536–1543.

23 Y. Zhao, X. Song, Q. Song and Z. Yin, A facile route to the synthesis copper oxide/reduced graphene oxide nano-

composites and electrochemical detection of catechol organic pollutant, *CrystEngComm*, 2012, **14**, 6710–6719.

24 Q. Bao, D. Zhang and P. Qi, Synthesis and characterization of silver nanoparticle and graphene oxide nanosheet composites as a bactericidal agent for water disinfection, *J. Colloid Interface Sci.*, 2011, **360**, 463–470.

25 G. Zhao, J. Li, X. Ren, J. Hu, W. Huc and X. Wang, Highly active MnO_2 nanosheet synthesis from graphene oxide templates and their application in efficient oxidative degradation of methylene blue, *RSC Adv.*, 2013, **3**, 12909.

26 P. H. Choi, K. W. Jun, S. J. Lee, M. J. Choi and K. W. Lee, Hydrogenation of carbon dioxide over alumina supported Fe-K catalysts, *Catal. Lett.*, 1996, **40**, 115–118.

27 T. Osaki, N. Narita, T. Horiuchi, T. Sugiyama, H. Masuda and K. Suzuki, Kinetics of reverse water gas shift (RWGS) disulfide catalysts reaction on metal disulfide catalysts, *J. Mol. Catal. A: Chem.*, 1997, **125**, 63–71.

28 G. Pekridis, K. Kalimeri, N. Kaklidis, E. Vakouftsi, E. F. Iliopoulou, C. Athanasiou and G. E. Marnellos, Study of the reverse water gas shift (RWGS) reaction over Pt in a solid oxide fuel cell (SOFC) operating under open and closed-circuit conditions, *Catal. Today*, 2007, **127**, 337–346.

29 H. C. Shin and S. C. Choi, Mechanism of M Ferrites (M=Cu and Ni) in the CO_2 Decomposition Reaction, *Chem. Mater.*, 2001, **13**, 1238–1242.

30 J. KaSpar, M. Graziani, A. M. Rahman, A. Trovarelli, E. J. S. Vichi and E. C. da Silva, Carbon dioxide hydrogenation over iron containing catalysts, *Appl. Catal., A*, 1994, **117**, 125–137.

31 Z. S. Fishman, B. Rudshteyn, Y. He, B. Liu, S. Chaudhuri, M. Askerka, G. L. Haller, V. S. Batista and L. D. Pfefferle, Fundamental Role of Oxygen Stoichiometry in Controlling the Band Gap and Reactivity of Cupric Oxide Nanosheets, *J. Am. Chem. Soc.*, 2016, **138**(34), 10978–10985.

32 U. Schwertmann, *Iron Oxides in the Laboratory: Preparation and Characterization*, *Rochelle M. Cornell*, 2nd, Completely Revised and Enlarged edn, 2000.

33 G. Kresse and J. Hafner, Ab initio molecular dynamics for liquid metals, *Phys. Rev. B: Condens. Matter*, 1993, **47**(1), 558–561.

34 G. Kresse and J. Hafner, Ab initio molecular-dynamics simulation of the liquid-metal-amorphous-semiconductor transition in germanium, *Phys. Rev. B: Condens. Matter*, 1994, **49**(20), 14251–14269.

35 G. Kresse and J. Furthmüller, Efficiency of *ab initio* total energy calculations for metals and semiconductors using a plane-wave basis set, *Comput. Mater. Sci.*, 1996, **6**(1), 15–50.

36 G. Kresse and J. Furthmüller, Efficient iterative schemes for ab initio total-energy calculations using a plane-wave basis set, *Phys. Rev. B: Condens. Matter*, 1996, **54**(16), 11169–11186.

37 P. E. Blöchl, Projector augmented-wave method, *Phys. Rev. B: Condens. Matter*, 1994, **50**(24), 17953–17979.

38 G. Kresse and D. Joubert, From ultrasoft pseudopotentials to the projector augmented-wave method, *Phys. Rev. B: Condens. Matter*, 1999, **59**(3), 1758–1775.

39 J. P. Perdew, K. Burke and M. Ernzerhof, Generalized Gradient Approximation Made Simple, *Phys. Rev. Lett.*, 1996, **77**(18), 3865–3868.

40 S. L. Dudarev, G. A. Botton, S. Y. Savrasov, C. J. Humphreys and A. P. Sutton, Electron-energy-loss spectra and the structural stability of nickel oxide: An LSDA+U study, *Phys. Rev. B: Condens. Matter*, 1998, **57**(3), 1505–1509.

41 F. N. Ponnamperuma, E. M. Tanco and T. Loy, Redox Equilibria in Flooded Soils: I. The Iron Hydroxide Systems, *Soil Sci.*, 1967, **103**(6), 374–382.

42 M. Ma, Y. Zhang, Z. Guo and N. Gu, Facile synthesis of ultrathin magnetic iron oxide nanoplates by Schikorr reaction, *Nanoscale Res. Lett.*, 2013, **8**, 16.

43 A. Weibel, R. Bouchet, F. Boulc' and P. Knauth, The Big Problem of Small Particles: A Comparison of Methods for Determination of Particle Size in Nanocrystalline Anatase Powders, *Chem. Mater.*, 2005, **17**, 2378–2385.

44 M. L. Pierce and C. B. Moore, Adsorption of Arsenite and Arsenate on Amorphous Iron Hydroxide, *Water Res.*, 1982, **16**(7), 1247–1253.

45 M. L. Pierce and C. B. Moore, Adsorption of Arsenite on Amorphous Iron Hydroxide from Dilute Aqueous Solution, *Environ. Sci. Technol.*, 1980, **14**(2), 214–216.

46 S. Fendorf, M. J. Eick, P. Grossl and D. L. Sparks, Arsenate and Chromate Retention Mechanisms on Goethite. 1. Surface Structure, *Environ. Sci. Technol.*, 1997, **31**(2), 315–320.

47 H. Fu and X. Quan, Complexes of fulvic acid on the surface of hematite, goethite, and akaganeite: FTIR observation, *Chemosphere*, 2006, **63**, 403–410.

48 U. Schwertmann and R. M. Cornell, *Iron Oxides in the Laboratory: Preparation and Characterization*, WileyVCH, New York, 2000, ch. 5 and 9.

49 Y. Wang, A. Muramatsu and T. Sugimoto, FTIR analysis of well-defined ~-Fe_2O_3 particles, *Colloids Surf., A*, 1998, **134**, 281–297.

50 A. P. Grosvenor, B. A. Kobe, M. C. Biesinger and N. S. McIntyre, Investigation of multiplet splitting of Fe 2p XPS spectra and bonding in iron compounds, *Surf. Interface Anal.*, 2004, **36**, 1564–1574.

51 T. Fujii, F. M. F. de Groot, G. A. Sawatzky, F. C. Voogt, T. Hibma and K. Okada, In situ XPS analysis of various iron oxide films grown by NO2-assisted molecular-beam epitaxy, *Phys. Rev. B: Condens. Matter*, 1999, **59**(4), 3195–3202.

52 P. C. J. Graat and M. A. J. Somers, Simultaneous determination of composition and thickness of thin iron-oxide films from XPS Fe 2p spectra, *Appl. Surf. Sci.*, 1996, **100–101**(2), 36–40.

53 NIST X-ray Photoelectron Spectroscopy Database, Version 4.1 (National Institute of Standards and Technology, Gaithersburg, 2012). https://srdata.nist.gov/xps/.

54 H. Abdel-Samad and P. R. Watson, An XPS study of the adsorption of chromate on goethite(a-FeOOH), *Appl. Surf. Sci.*, 1997, **108**, 371–377.

55 K. Sivula, F. Le Formal and M. Grätzel, Solar Water Splitting: Progress Using Hematite (a-Fe2O3) Photoelectrodes, *ChemSusChem*, 2011, **4**, 432–449.

56 B. Gilbert, C. Frandsen, E. R. Maxey and D. M. Sherman, Band-gap measurements of bulk and nanoscale hematite by soft x-ray spectroscopy, *Phys. Rev. B: Condens. Matter*, 2009, **79**, 035108.

57 L. A. Marusai, R. Messier and W. B. White, Optical Absorption Spectrum of Hematite, αFe_2O_3 Near IR to UV, *J. Phys. Chem. Solids*, 1980, **41**(9), 981–984.

58 R. Van de Krol, J. Ségalini and C. S. Enache, Influence of point defects on the performance of InVO4 photoanodes, *J. Photonics Energy*, 2011, **1**(1), 016001.

59 D. M. Sherman, Electronic structures of iron(III) and manganese(IV) (hydr)oxide minerals: Thermodynamics of photochemical reductive dissolution in aquatic environments, *Geochim. Cosmochim. Acta*, 2005, **69**(13), 3249–3255.

60 R. A. Dictor and A. T. Bell, Fischer-Tropsch synthesis over reduced and unreduced iron oxide catalysts, *J. Catal.*, 1986, **97**(1), 121–136.

61 T. F. Jaramillo, K. P. Jørgensen, J. Bonde, J. H. Nielsen, H. Sebastian and I. Chorkendorff, Identification of Active Edge Sites for Electrochemical H2 Evolution from MoS_2 Nanocatalysts, *Science*, 2007, **317**.

62 M. S. Spencer, On the activation energies of the forward and reverse water-gas shift reaction, *Catal. Lett.*, 1995, **32**, 9–13.

63 A. B. Getsoian, Z. Zhai and A. T. Bell, Band-Gap Energy as a Descriptor of Catalytic Activity for Propene Oxidation over Mixed Metal Oxide Catalysts, *J. Am. Chem. Soc.*, 2014, **136**(39), 13684–13697.